

Synthesis, Structure, Texture, and CO Sensing Behavior of Nanocrystalline Tin Oxide Doped with Scandia

Gang Xu,[†] Ya-Wen Zhang,* Xiao Sun, Chang-Liang Xu, and Chun-Hua Yan*

State Key Laboratory of Rare Earth Materials Chemistry and Applications, PKU-HKU Joint Laboratory on Rare Earth Materials and Bioinorganic Chemistry, Peking University, Beijing 100871, China

Received: October 15, 2004; In Final Form: December 11, 2004

Weakly agglomerated nanocrystalline scandia doped tin oxide powders with high surface area (170–220 m²/g) and uniform size (3–4 nm) were synthesized for the first time by a two-step hydrothermal process in the presence of urea, followed by the calcination between 500 and 1200 °C. The structure and texture of the binary oxide system were characterized by thermogravimetry and differential thermal analysis, Brunauer–Emmett–Teller-specific surface area analysis, transmission electron microscopy, X-ray diffraction, Raman spectroscopy, and X-ray photoelectron spectroscopy. A metastable scandium tin oxide solid solution in tetragonal structure was formed for the scandia content lower than 6 mol % as the samples were calcined at 800 °C, and the excess Sc atoms were dispersed at the surface of the crystallites above this limit. The solid solution was metastable, so scandium migrated toward the surface region of the crystallites and produced a second phase of Sc₄Sn₃O₁₂ during calcining at high temperatures over 1000–1200 °C. In the case of the samples with higher dopant concentration (> 15 mol %), the calcination at the temperature between 500 and 800 °C caused the precipitation of Sc₂O₃, and the calcination over 1000–1200 °C led to the formation of more Sc₄Sn₃O₁₂. Textural analysis showed that doping an appropriate amount of Sc₂O₃ into nanosized SnO₂ could effectively inhibit the grain growth and stabilize the surface area against high-temperature calcinations below 1000 °C. CO gas-sensing property measurements revealed that the dispersion of Sc at the surfaces of the SnO₂ nanocrystallites could improve the CO sensitivity significantly, and the pellet sample with scandia content of 10 mol % sintered at 800 °C showed the best CO gas-sensing property in the operation temperature range of 300–400 °C. On the basis of the structural and textural analysis, the correlation between the structure/texture and the sensitivity to CO for the as-calcined (SnO₂)_{1-x}(Sc₂O₃)_x nanocrystallites has been established and explained.

Introduction

SnO₂ is an *n*-type semiconductor with a direct band gap of 3.6 eV between the full oxygen 2p valence band and the tin states at the bottom of the conduction band and has received intensive interest for its applications in solar cells,^{1,2} catalysis,³ and transparent electrodes,⁴ especially in combustible and toxic gas detection devices (gas sensors).^{5,6} For most of these applications, using nanocrystalline SnO₂ with high stability (in terms of grain size, surface area, and the amount of active sites) against sintering/aging during heat-treatment steps or during their use at high temperatures is regarded as a promising way to fabricate the catalytic and electronic devices (such as gas sensors) with superior performance.

As is well-known, the basis of the sensor application is the modification of the conductivity of the metal oxide by adsorption of gases from the atmosphere. Catalytic reaction between reducing species and surface-adsorbed oxygen at elevated temperatures releases carriers in the conduction band and thus makes changes in conductivity of the gas sensors. The use of nanoparticulate SnO₂ in the gas sensors has been shown to enhance the device performance due to the characteristic microstructural and electronic properties of the specific SnO₂

nanostructure. For example, high specific surface areas of the SnO₂ nanoparticles can lead to an increase in active surfaces for sensing, and the small size of the nanoparticles can be manipulated to be compatible with the thickness of the electron depletion layer (about 3 nm). Under these conditions, neck- or grain-controlled sensing action and hence enhanced sensitivity can be achieved.⁷ However, the main problems with gas sensors based on pure SnO₂ are the stability at high operation temperature, low sensitivity, and poor selectivity.

For decades, many attempts have been made for improving the sensing properties of SnO₂ gas sensors in order to fit the increasing demands of sensors to work in more complicated systems and under more strict conditions. Recently, doping and catalytic modifiers are frequently used to improve the performance of SnO₂ sensors. Noble metals, such as Pt and Pd, are known to promote the chemical reactions occurring at the oxide surface, which can increase sensitivity, selectivity, and response speed of sensors.^{8,9} Bulk doping with various metal oxides is another common method to improve the sensitivity of SnO₂-based sensors. Numerous transition-metal oxides (e.g., CuO, Co₃O₄, Fe₂O₃, Mn₂O₃, MoO₃)^{10–14} and rare-earth oxides (e.g., Y₂O₃, La₂O₃, CeO₂)^{15–18} acting as dopants have been reported in much of the literature. However, the “trial-and-error” method is still mainly used in the search of new sensor materials or suitable additives to modify the existing sensor materials. To guide for the search of better SnO₂ sensor materials, it is necessary to understand the physicochemical and structural

* Authors to whom correspondence may be addressed. Tel. and Fax: +86-10-62754179. E-mail: yan@pku.edu.cn (C.-H.Y.).

[†] Present address: Institute of Nuclear and New Energy Technology, Tsinghua University, Beijing 100084, China.

characteristics of various mixed oxides especially in the nanometric regime with respect to either the preparation technique or the doping components. Therefore, a comprehensive understanding of the relationships between structure/texture and properties is essential in the development of novel SnO₂ nanostructure with exceptional performance for sensor applications.

Tin oxide powder is the starting material to make SnO₂ ceramic sensors, and the preparative method remarkably affects the degree of crystallinity, crystallite size, phase composition, density of lattice defects, and the surface structure of the as-derived powders. These in turn determine the characteristics and performances of the eventual sensors. So far, many techniques, including the sol–gel method,¹⁵ polymeric precursor route,^{17,18} chemical precipitation,^{16,19,20} direct oxidation through gas-phase condensation,^{21,22} tin salt decomposition,^{23,24} and chemical vapor deposition (CVD) methods, have been developed to fabricate ultrafine SnO₂ powders.²⁵ More recently, the doping of rare-earth oxides (Y₂O₃, La₂O₃, CeO₂) into SnO₂ either by the sol–gel method or polymeric precursor route has been demonstrated not only to effectively inhibit the particle growth against high-temperature sintering and thus to considerably stabilize the surface area of nanocrystalline SnO₂ but also to enhance the gas sensing and catalytic properties, due to the doping-induced modification of the amount of the active sites on the surfaces of the nanoparticles.^{15,17,18} Such a modification effect may arise from not only the lanthanide contraction induced monotonic change of ionic radii, but also the different stable oxidation states and the variation in chemical reactivity (such as basicity).

Among the trivalent rare earths, Sc³⁺ has the smallest ionic size ($r_{VI} = 0.89 \text{ \AA}$),²⁶ close to that of Sn⁴⁺ ($r_{VI} = 0.83 \text{ \AA}$),²⁶ and its hydroxide is the most basic. In particular, scandium oxide possesses high heat resistance ($M_p = 2485 \text{ }^\circ\text{C}$). In this research, for the first time to our knowledge, nanocrystalline tin oxide powders doped with scandia were synthesized by a mild urea-based hydrothermal approach we developed not long ago.^{27,28} In this paper, the doping effects of scandia on the structure, texture, and CO sensing property of the nanocrystalline SnO₂ synthesized by the above hydrothermal route are presented. The (SnO₂)_{1-x}(Sc₂O₃)_x ($x = 0\text{--}0.6$) system exhibits interesting structural characteristics depending upon the dopant concentration. As the Sc content increases, the formation of metastable SnO₂–Sc₂O₃ solid solution, the dispersing of Sc on the surfaces of SnO₂ grains, and the segregation of an individual Sc–Sn compound (Sc₄Sn₃O₁₂) can be orderly observed for the as-prepared nanocrystalline (SnO₂)_{1-x}(Sc₂O₃)_x powders during high-temperature calcinations over 500–1200 °C. We also observe that doping an appropriate amount of Sc₂O₃ into nanosized SnO₂ can not only improve its textural properties (inhibiting particle growth and stabilizing surface area against high-temperature calcinations) but also can enhance its CO sensing behavior. On the basis of the structural and textural analysis, the correlation between the structure/texture and the sensitivity to CO for the as-calcined (SnO₂)_{1-x}(Sc₂O₃)_x nanocrystallites is manifested in this paper.

Experimental Section

1. Synthesis. The nanocrystalline (SnO₂)_{1-x}(Sc₂O₃)_x ($x = 0\text{--}0.6$) powders were prepared by a two-step urea-based hydrothermal method.^{27,28} Stoichiometric solutions of SnCl₂·5H₂O (analytical-reagent grade, Beijing Chemical Plant, Beijing, PRC), Sc(NO₃)₃ (99.95%, Zhaoqing Nonferrous Metals and Industry Corp., Guangdong, PRC), and urea (analytical-reagent

grade, Beijing Chemical Plant, Beijing, PRC) in the molar ratio of (Sn²⁺ + Sc³⁺):urea = 1:4 were employed to prepare the stock solution (85 mL) with a cation concentration of 0.05 mol L⁻¹ in a Teflon (DuPont, Wilmington, DE) cup (100 mL). The cup was then transferred into a stainless steel autoclave and subjected to hydrothermal treatment at 80 °C for 6 h and subsequently at 180 °C for another 24 h under autogenous pressure in an electric oven. As the autoclave cooled to room temperature naturally, the precipitated powders were filtered, washed with deionized water and ethanol, and dried in a vacuum oven at about 60 °C. The as-prepared powders were then calcined in a muffle furnace at 500–1200 °C for 2 h under stagnant air with a heating rate of 20 °C/min and a cooling rate of 5 °C/min.

The as-prepared Sc₂O₃-doped SnO₂ powders were uniaxially pressed at around 130 MPa to form pellets with a diameter of 6 mm and a thickness of 2 mm, and were then sintered at 800 °C for 24 h in air. Two Pt lead wire electrodes were adhered to two sides of the pellet sample with Pt paste, which was fired at 800 °C for 10 min to remove the polymeric components. The sensor material was then “initialized” by heating it at 400 °C for 48 h in clean and dry air. This initialization procedure was found to be necessary to obtain reproducible response to CO.

2. Characterization Methods. The crystal structures were identified by a powder X-ray diffractometer (XRD, Rigaku D/max-2000, Tokyo, Japan), employing Cu K α radiation ($\lambda = 1.5418 \text{ \AA}$). The XRD data of powder samples calcined at 800 °C for Rietveld refinement were collected from 20 to 80° with a 2θ speed of 1°/min on the same diffractometer. The data were analyzed using the software of General Structure Analysis System (GSAS) to obtain the lattice parameters.²⁹ The average grain size D of tetragonal SnO₂ was estimated according to the Scherrer equation³⁰

$$D = \frac{0.99\lambda}{\beta \cos \theta} \quad (1)$$

where θ is the diffraction angle of the (110) peak of the tetragonal phase and β is the full width at half maximum (fwhm) of the (110) peak (in radian), which is calibrated from high purity silicon. The microstrain in the as-calcined nanocrystallites was estimated by the single line method for analysis of XRD line broadening using a Pseudo-Voigt profile function.³¹

The combined thermogravimetry and differential thermal analysis (TG-DTA, SDT2960, Thermal Analysis) was performed at a heating rate of 10 °C min⁻¹ from room temperature to 1000 °C, using α -Al₂O₃ as a reference. The Brunauer–Emmett–Teller (BET)-specific surface area was measured by nitrogen physisorption at 77.5 K using an ASAP 2010 analyzer (Micromeritics Co. Ltd., Norcross, USA). FT-IR spectra were obtained on a Nicolet Magna 750 FTIR spectrometer at a resolution of 4 cm⁻¹ with a Nic-Plan IR Microscope. Vis–Raman spectra were determined on a Renishaw (U.K.) spectrometer with an Ar ion laser of 514.5-nm excitation wavelength. Backscattering geometry was adopted for the measurement under the conditions of a laser power of 20 mW and a resolution of 4 cm⁻¹. Surface composition was determined by X-ray photoelectron spectroscopy (XPS) in an ion-pumped chamber (evacuated to 1.3×10^{-8} Torr) of Axis Ultra (U.K.) spectrometer equipped with a focused monochromatized X-ray source (Al K α , $h\nu = 1486.6 \text{ eV}$) at a power of 225 W. A hemispherical analyzer collected the photoelectrons at an angle of 90° from the surface. The binding energy (BE) for the samples was calibrated by setting the measured BE of C 1s to 284.8 eV. The standard error of the quantitative analysis is about 20%. Transmission electron microscopy (TEM) measurements were

conducted employing a JEOL 200CX electronic microscope working at 200 kV. High-resolution TEM (HRTEM) characterization was performed with a Philips Tecnai F30 FEG-TEM (FEI Company, Hillsboro, OR) operated at 300 kV. Samples for TEM and HRTEM were obtained by dispersing a small drop of the suspension with much lower concentration onto a copper grid precoated with amorphous carbon.

3. CO Gas-Sensing Measurements. The sensors were tested using a fully computer-controlled gas sensor test rig. CO gas was supplied by Huayuan Gas Corp. of China (0.2% CO in air), and this was diluted with clean and dry air as necessary to provide a wide range of pollutant gas concentrations. The flow rate of the gases was kept at 200 mL/min throughout the measurement using mass flow controllers.

Complex impedance measurements were carried out from 0.5 to 10^7 Hz using a Solartron frequency response analyzer Model SI 1260 with a dielectric interface 1296. Automated acquisition was facilitated by ZPlot Version 2.401 (Scribner Associates) software. The impedance data were analyzed with the software ZView Version 2.401 (Scribner Associates) and were fitted by an equivalent circuit, i.e., two parallel circuits of a resistance and a constant phase element (CPE) in series. Thus the resistances of the bulk (R_b) and the grain boundary (R_{gb}) can be obtained. The total resistance (R) of the sample is the sum of R_b and R_{gb} . The conductance of the sensors was measured every 5 s. A temperature profile of sensitivity was obtained to identify the temperature of maximum response to CO by exposing the sensors to fixed concentrations of CO (1000 ppm) at varying operation temperatures (250–450 °C). The sensors were typically exposed to 600-s pulses of CO followed by 600-s reversal in clean and dry air, and the sensitivity (S) is determined by

$$S = R_{\text{air}}/R_{\text{CO}} \quad (2)$$

where R_{air} is the resistance of the sensor in dry air, and R_{CO} is the resistance in CO.

Results and Discussion

1. Synthesis Process. As a mild process, urea hydrolysis takes place in the stock solution containing homogeneously distributed urea and metal ions upon heating and can be quickly stopped at a desired pH by cooling the reaction solution to room temperature. During the urea hydrolysis, the precipitates are formed via homogeneous nucleation. The nucleation and crystallite growth are thus readily controlled by adjusting the hydrolysis speed and the resultant pH. More recently, we employed a two-step hydrothermal urea homogeneous precipitation method²⁷ to synthesize nanocrystalline rare earth stabilized zirconia powders with well-controlled compositions and microstructures (crystallite size, size distribution, and surface area) via a heterogeneous nucleation-growth mechanism involving three stages:²⁸ (i) the formation of polymeric hydroxide complexes between the Zr and rare earth species under the hydrolysis of urea, (ii) the formation of hydrous oxide with an ordered structure similar to a cubic structure by dissolution and reprecipitation upon aging at a low temperature of 80–90 °C, and (iii) the in situ transformation of the hydrous oxide into anhydrous oxide and full crystallization via dissolution–recrystallization under hydrothermal treatment at a high temperature of 180 °C. By this two-step hydrothermal method, weakly agglomerated and homogeneous nanocrystalline rare earth stabilized zirconia powders with high size uniformity and good stability against particle growth during high-temperature calcination have been obtained.

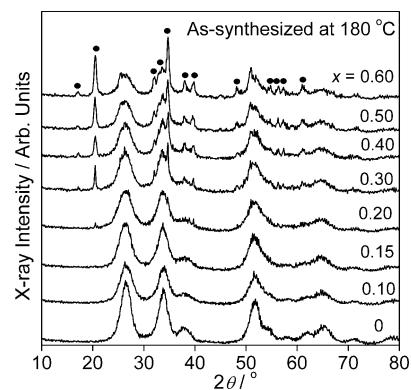


Figure 1. XRD patterns of the as-synthesized $(\text{SnO}_2)_{1-x}(\text{Sc}_2\text{O}_3)_x$ ($x = 0-0.6$) powders. (●) Orthogonal α -ScOOH (JCPDS 20-1035, $Pbnm$).

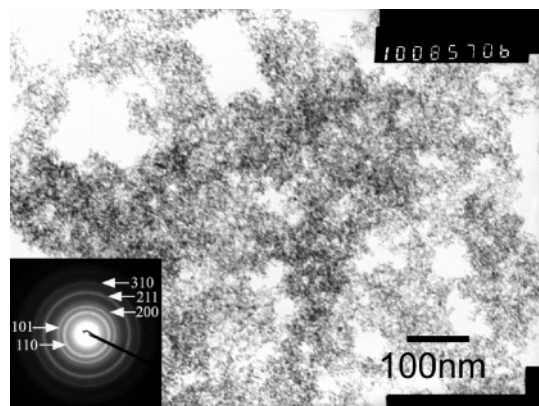


Figure 2. TEM image of the as-synthesized $(\text{SnO}_2)_{0.92}(\text{Sc}_2\text{O}_3)_{0.08}$ powder. Inset is the SAED.

In the present work, for preparing weakly agglomerated nanocrystalline $(\text{SnO}_2)_{1-x}(\text{Sc}_2\text{O}_3)_x$ powders with well-controlled compositions, the two-step hydrothermal treatment in the presence of urea was also used. When heating at 80 °C, homogeneous nucleation would happen to form a (Sn,Sc) hydroxide precipitate, and then the precipitate was further hydrothermally treated at 180 °C for obtaining highly crystallized $(\text{SnO}_2)_{1-x}(\text{Sc}_2\text{O}_3)_x$ powders with less phase segregation. The concentrations of metal ions and urea were screened and fixed at 0.05 and 0.2 mol/L, respectively. The final pH values of the reaction solutions were around 9.5. Under this condition, both Sn^{4+} (for $\text{Sn}(\text{OH})_4$, $\text{p}K_{\text{sp}} = 56$) and Sc^{3+} (for $\text{Sc}(\text{OH})_3$, $\text{p}K_{\text{sp}} = 30.65$) ions can completely hydrolyze during hydrothermal treatment, so as to ensure the final products to appear at expected compositions.

2. Characteristics of the As-Synthesized Nanocrystallites. Figure 1 shows the XRD patterns of the as-synthesized $(\text{SnO}_2)_{1-x}(\text{Sc}_2\text{O}_3)_x$ ($x = 0-0.6$) powders, from which it is observed that the main diffraction peaks are broadened, and can be indexed as tetragonal SnO_2 (JCPDS 41-1445, $P42_1/mnm$). When the Sc_2O_3 dopant content (x) exceeds 0.2, a second phase (orthogonal α -ScOOH, JCPDS 20-1035, $Pbnm$) appears. The primary particles of the as-synthesized $(\text{SnO}_2)_{1-x}(\text{Sc}_2\text{O}_3)_x$ nanocrystallites are highly uniform and well-dispersed with a crystallite size of less than 5 nm (see the typical TEM image of the sample with $x = 0.08$ shown in Figure 2). The selected area electron diffractions (SAED), shown in the inset of Figure 2, confirmed the formation of tetragonal SnO_2 nanocrystals for the as-synthesized $(\text{SnO}_2)_{0.92}(\text{Sc}_2\text{O}_3)_{0.08}$.

Figure 3 shows the typical combined TG-DTA run of the as-synthesized $(\text{SnO}_2)_{0.96}(\text{Sc}_2\text{O}_3)_{0.04}$ powders, indicating a two-step weight loss process on the TG curve. The first weight loss

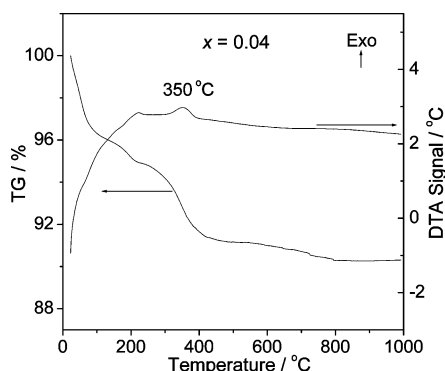


Figure 3. Combined TG-DTA run of the as-synthesized $(\text{SnO}_2)_{0.96}-(\text{Sc}_2\text{O}_3)_{0.04}$ powders.

beginning from 25 to 200 °C could be attributed to the liberation of physically adsorbed water and ethanol molecules, and the second one between 200 and 400 °C could be ascribed to the elimination of residuals through oxidation–reduction reaction. However, no obvious exothermic (exo) peak for the transition from amorphous to crystalline at the temperature of 400–500 °C is detected,³² indicating that the hydrolytic products have already been well crystallized. We observed a weight loss of ca. 4% for the first step and 8–10% for the second step in the x range of 0–0.15. It should be noted that the exothermic peak for the second step increased monotonically from ca. 335 °C for $x = 0$ to ca. 374 °C for $x = 0.15$, indicating that the more Sc_2O_3 doped into SnO_2 the more contaminants remained in the as-synthesized nanocrystalline powders.

3. Structure of the As-Calcined Nanocrystallites. The XRD patterns of $(\text{SnO}_2)_{1-x}(\text{Sc}_2\text{O}_3)_x$ ($x = 0-0.60$) powders calcined at 500 and 800 °C are shown in Figure 4. When calcined at 500 °C, cubic Sc_2O_3 (JCPDS 42-1463, $Ia\bar{3}$) appears as $x > 0.2$ (Figure 4a), while for the samples calcined at 800 °C, cubic Sc_2O_3 appears as $x > 0.15$ (Figure 4b). As the dopant content below the threshold value mentioned above, only tetragonal SnO_2 can be indexed. An interesting phenomenon is also observed from Figure 4 that the (110) peak of SnO_2 becomes more broadened while other peaks such as (101) and (211) seem to be narrowed accompanied with more segregated Sc_2O_3 , indicating that the crystal growth of SnO_2 along the crystal facet (110) has been suppressed at high level doping of Sc_2O_3 .

Figure 5 shows the relationship between the content ratio of Sc_2O_3 to SnO_2 calculated from XRD and the composition ratio in the as-calcined $(\text{SnO}_2)_{1-x}(\text{Sc}_2\text{O}_3)_x$ powders. It is revealed that the content ratio of Sc_2O_3 to SnO_2 varies linearly under the calcination temperatures of both 500 and 800 °C, indicating the proportional segregation of Sc_2O_3 crystals at the high dopant

content. The intersection of the straight lines with the x axis is called a threshold value, which represents the maximum dopant content.³³ The derived threshold values are 0.26 and 0.13 $\text{Sc}_2\text{O}_3/\text{SnO}_2$ (g/g) for $\text{SnO}_2-\text{Sc}_2\text{O}_3$ system calcined at 500 and 800 °C, respectively, corresponding to the molar ratio of Sc_2O_3 , 0.22 and 0.12, respectively. The reduction of the threshold for the calcination at 800 °C, compared with that at 500 °C, probably indicates the metastable nature of the $\text{SnO}_2-\text{Sc}_2\text{O}_3$ nanocomposites.

As shown in Figures 4b and 5, the nanocrystalline $(\text{SnO}_2)_{1-x}(\text{Sc}_2\text{O}_3)_x$ powders calcined at 800 °C exhibit pure tetragonal structure in the x range of 0–0.15. To determine the precise structure of the binary system as $x < 0.15$, Rietveld refinement, Raman spectroscopy, as well as X-ray photoelectron spectroscopy are used to characterize the powders calcined at 800 °C. The $(\text{SnO}_2)_{1-x}(\text{Sc}_2\text{O}_3)_x$ ($x = 0-0.15$) powders calcined at 800 °C for 24 h were applied for the Rietveld refinement. The powder XRD patterns of the as-calcined samples were fitted with the GSAS program. All patterns can be indexed to tetragonal SnO_2 and are fitted with the space group $P4_2/mnm$ except that a bit of the noisy phase of cubic Sc_2O_3 can be found when $x = 0.15$ (see Figure 1S). The diffraction peaks are greatly broadened when x is greater than 0.02 (Figure 1S) and thus brings relative large fitting error of R_p in the range of 7–11%. The variations of the refined lattice parameters a vs Sc_2O_3 content are drawn in Figure 6a. It is shown that the lattice parameter a increases linearly in the x range of 0–0.06 and becomes a constant when $0.06 < x < 0.15$. However, the lattice parameter c changes scarcely considering the fitting errors (see Figure 6b). The variation of the lattice parameter a thus suggests that the $(\text{SnO}_2)_{1-x}(\text{Sc}_2\text{O}_3)_x$ binary system might be in a solid solution structure at low Sc_2O_3 content, and the solution limit is $x = 0.06$. When the dopant content exceeds the solid solution limit of $x = 0.06$, excess Sc could be segregated from the SnO_2 lattice.

As is well-known, Raman spectroscopy is an effective method for analyzing the crystal structure of fine particles, and many studies have focused on the Raman scattering of crystalline SnO_2 .^{34–37} SnO_2 with the tetragonal structure belongs to the space group D_{4h}^{14} , of which the normal lattice vibration at the Γ point of the Brillouin zone is given as follows on the basis of group theory (Porto et al.³⁸)

$$\Gamma = 1A_{1g} + 1A_{2g} + 1A_{2u} + 1B_{1g} + 1B_{2g} + 2B_{1u} + 1E_g + 3E_u \quad (3)$$

Among these vibrations, the modes A_{2u} and E_u are infrared active and the modes A_{1g} , B_{1g} , B_{2g} , and E_g are Raman active, while the mode B_{1u} is optically inactive. Figure 7a shows the

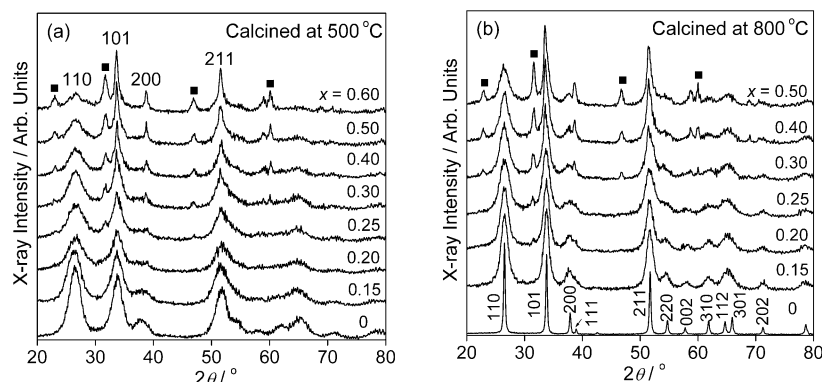


Figure 4. XRD patterns of the $(\text{SnO}_2)_{1-x}(\text{Sc}_2\text{O}_3)_x$ ($x = 0-0.6$) powders. (a) Calcined at 500 °C for 2 h; (b) calcined at 800 °C for 2 h. (■) Cubic Sc_2O_3 (JCPDS 42-1463, $Ia\bar{3}$).

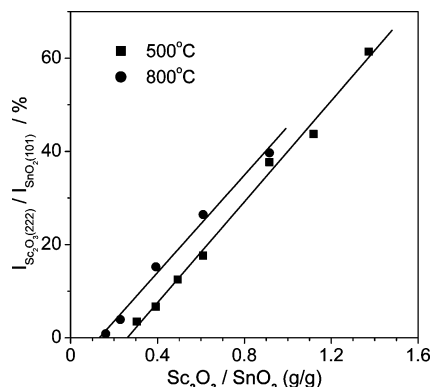


Figure 5. The content ratio of Sc_2O_3 to SnO_2 calculated from the XRD patterns of the $(\text{SnO}_2)_{1-x}(\text{Sc}_2\text{O}_3)_x$ powders calcined at (■) 500 °C and (●) 800 °C for 2 h vs the composition ratio.

Raman spectra of the $(\text{SnO}_2)_{1-x}(\text{Sc}_2\text{O}_3)_x$ ($x = 0-0.15$) powders calcined at 800 °C. Raman intensity is the strongest for the mode A_{1g} at 633 cm^{-1} for the sample with $x = 0$, followed by the mode B_{2g} at 775 cm^{-1} and the mode E_g at 475 cm^{-1} . The data of A_{1g} , B_{2g} , and E_g modes are in agreement with those observed in a previous report.³⁹ These three modes are also indicative of the high crystallinity of the powders.³⁴ The Raman spectra of $x = 0.02-0.08$ also show the typical features of the tetragonal SnO_2 . However, for $x = 0.1$, the Raman intensities are much weaker due to a strong fluorescence disturbance. The Raman peaks of $x = 0.15$ are quite different from those of $x < 0.1$. The Raman peaks belonging to cubic Sc_2O_3 are found for $x = 0.15$, which is in accordance with the result of XRD (see Figure 4b).

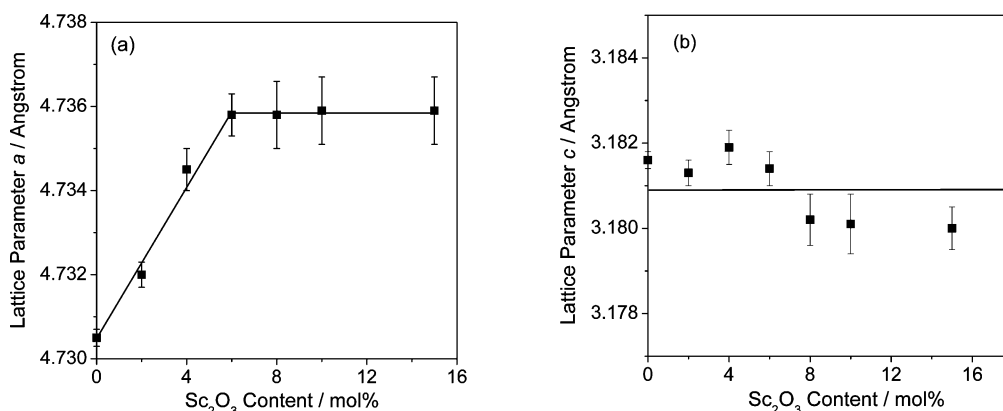


Figure 6. Lattice parameters a (a) and c (b) of the nanocrystalline $(\text{SnO}_2)_{1-x}(\text{Sc}_2\text{O}_3)_x$ ($x = 0-0.15$) powders calcined at 800 °C for 24 h.

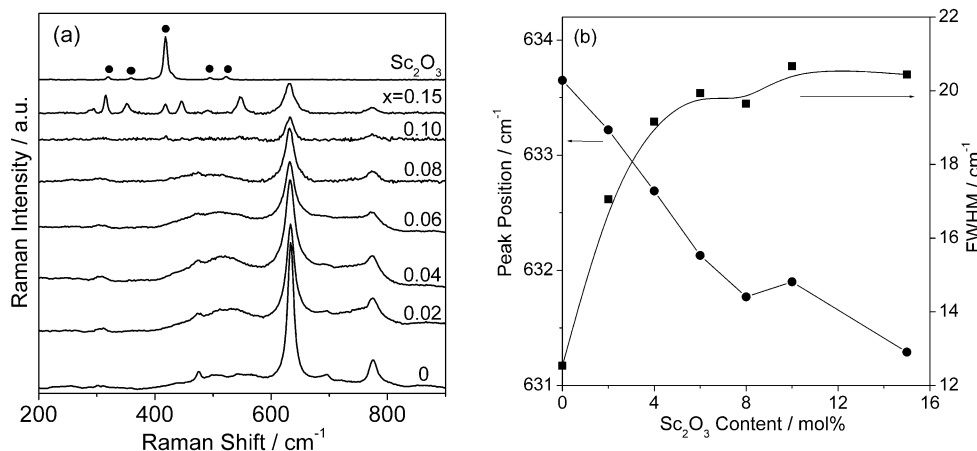


Figure 7. (a) Raman spectra of the nanocrystalline $(\text{SnO}_2)_{1-x}(\text{Sc}_2\text{O}_3)_x$ ($x = 0-0.15$) powders calcined at 800 °C for 2 h. (The Raman spectrum of Sc_2O_3 is also given for reference.) (b) Raman peak position and fwhm of the Sn—O A_{1g} bond vs the Sc_2O_3 content.

Raman peak position and the fwhm of the Sn—O A_{1g} bond vs Sc_2O_3 content are shown in Figure 7b. The Raman peak position reduces linearly from $x = 0$ to 0.08, exhibiting a red shift. Abello et al.³⁵ studied the structure of nanocrystalline SnO_2 by Raman spectroscopy and found that the frequency of the Raman modes systematically decreased with the crystallite size. The red shift could be interpreted on the basis of a tensile state that should develop progressively in the bulk of crystallites when their surface contribution increases. At the present study, the linear red shift of the Raman peaks is probably due to the weakening of the Sn—O bond as a result of the expansion of crystal lattice (see Figure 6a). The fwhm of the peak increases dramatically from 12.5 cm^{-1} for $x = 0$ to 20 cm^{-1} for $x = 0.06$ and varied a little as $x > 0.06$ (also see Figure 7b). The broadening of the A_{1g} peak with an increase in the dopant content (decreasing of the grain size) indicates an increase in the density of lattice defects.³⁴ Furthermore, the band appearing around 540 cm^{-1} is not commonly observed in the Raman spectra of single crystal and polycrystalline SnO_2 and is only visible for nanosized SnO_2 grains. This band is interpreted as the effect of surface phonon modes, which dominates when the crystallite size is small enough, i.e., a size effect.^{36,37} With the decrease of crystallite size, the ratio of surface atoms vs volume atoms increases, and thus the contribution of the surface phonons increases compared to that from the volume phonons.

The XPS spectra were measured for the $(\text{SnO}_2)_{1-x}(\text{Sc}_2\text{O}_3)_x$ ($x = 0-0.50$) powders calcined at 800 °C for 2 h (typically see Figure 2S). The atomic ratio of Sc/Sn on the surface of the samples, calculated from the XPS peak area ratio of Sc 2p and Sn 3d bands, is shown in Figure 8. For $x < 0.04$, the Sc/Sn

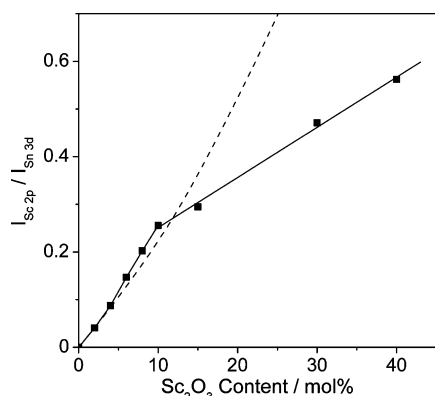


Figure 8. XPS quantitative results of Sc/Sn for $(\text{SnO}_2)_{1-x}(\text{Sc}_2\text{O}_3)_x$ ($x = 0\text{--}0.5$) powders calcined at 800 °C for 2 h. The dash line indicates the bulk composition.

ratio on the surface is similar to that of the bulk composition, exhibiting the characteristic of solid solution, which is also proved by the lattice parameter refinement (see Figure 6a) and Raman spectroscopy (Figure 7b). As the dopant content of Sc_2O_3 increases, more Sc atoms are found on the surface, and a turning point was obtained for $x = 0.10$, beyond which the Sc/Sn ratio on the surface is much lower than the corresponding bulk composition.

Note that no crystalline Sc_2O_3 was detected for $x = 0.10$ calcined at 800 °C by both XRD (Figure 4b) and Raman spectroscopy (Figure 7a), the segregated Sc might have dispersed on the surface of SnO_2 grains. Since cubic Sc_2O_3 is detected for $x > 0.15$, the reduction of the surface Sc is due to the core formation of Sc_2O_3 , leading to lower Sc/Sn ratios on the surface than those of the bulk. The segregation of the dopant (e.g., Cu,^{40,41} Fe,⁴¹ Sb^{42,43}) from the SnO_2 lattice to the surface of the grains has been reported recently. Briois et al.⁴⁰ studied the structure of the sol–gel-derived nanocrystalline copper-doped tin oxide by extended X-ray absorption fine structures and found that a metastable copper tin oxide substitutional solid solution was formed for copper doping lower than 1 mol %. Above this limit, the excess copper was adsorbed at the surface of the crystallite. Moreover, the dopants would gradually move to the surface regions of the crystallites on heating.^{40,41} According to the above discussion, similar conclusions can also be drawn in the present $(\text{SnO}_2)_{1-x}(\text{Sc}_2\text{O}_3)_x$ system. A solid solution of scandium tin oxide is formed for the samples with $x < 0.06$ after calcining at 800 °C, excess Sc remains adsorbed at the surface of the SnO_2 grains as x exceeds the limit of 0.06. For higher dopant concentrations ($x > 0.15$), Sc will be dispersed in saturation and segregated as individual phase of Sc_2O_3 . When the $(\text{SnO}_2)_{1-x}(\text{Sc}_2\text{O}_3)_x$ powders are calcined at even higher

temperatures (> 800 °C), an interesting phenomenon is found. From the XRD patterns shown in Figure 9, a compound $\text{Sc}_4\text{Sn}_3\text{O}_{12}$ is observed as $x > 0.06$ and $x > 0.02$ for the samples calcined at 1000 and 1200 °C, respectively. The possible explanation is that the solid solution is metastable, so that the dopant Sc inclines to move to the surface region SnO_2 crystallites and react with SnO_2 to produce $\text{Sc}_4\text{Sn}_3\text{O}_{12}$ under high-temperature calcinations.

4. Texture of the As-Synthesized and Calcined Nanocrystallites. The average crystallite size of $(\text{SnO}_2)_{1-x}(\text{Sc}_2\text{O}_3)_x$ powders in the x range of 0–0.15, calculated by the Scherrer equation, is shown in Figure 10. It is noted that the crystallite sizes of the as-synthesized nanocrystals are all around 3–4 nm, which scarcely increase by the calcination below 500 °C, especially for the samples with $x > 0.04$. When calcined at 800 °C, the pure SnO_2 ($x = 0$) sample shows a sudden grain coarsening, and has an average crystallite size of 31 nm. However, the doped samples grow slowly, and their average crystallite sizes decrease with the increase of x , from 11 nm for $x = 0.02$ to 5 nm for $x = 0.15$. The dependence of the crystallite size on the Sc concentration indicates that the grain growth tends to be effectively inhibited by the doping of more Sc_2O_3 .

Figure 11 depicts the BET surface area of the nanocrystalline $(\text{SnO}_2)_{1-x}(\text{Sc}_2\text{O}_3)_x$ ($x = 0\text{--}0.5$) powders. It is noted that the BET specific surface areas of the as-synthesized powders are as large as 170–220 m²/g for $x = 0\text{--}0.15$ and decrease along with the calcination temperature. It is also noted that the specific surface area of pure SnO_2 ($x = 0$) drops from 170 m²/g for the as-synthesized powder to 80 m²/g at the calcination temperature of 500 °C and to only 12 m²/g when calcined at 800 °C. With increasing x in the range of 0–0.2, the average crystallite size reduces (Figure 10) and the surface area thus increases obviously. For $x = 0.1$, the specific surface area is varied from 221 m²/g for the as-synthesized sample to 120 m²/g and 56 m²/g at the calcination temperature of 500 and 800 °C, respectively. However, the specific surface area becomes reduced to a fixed value as $x > 0.2$ for the as-calcined samples due to the segregation of the cubic Sc_2O_3 crystals (see Figure 4). From Figure 11, we can also find that the doping of an appropriate portion of Sc_2O_3 ($x = 0.08\text{--}0.2$) can markedly improve the stability of surface area against high-temperature calcination due to the effective inhibition of grain growth by the doping of Sc_2O_3 at this dopant range. Additionally, in comparison with the case for the as-synthesized samples, the average crystallite size of the as-calcined samples at 500 °C did not change much (see Figure 10), while their surface areas had a dramatic difference (see Figure 11), perhaps indicating that a significant interparticle aggregation occurred during the calcination at this temperature.

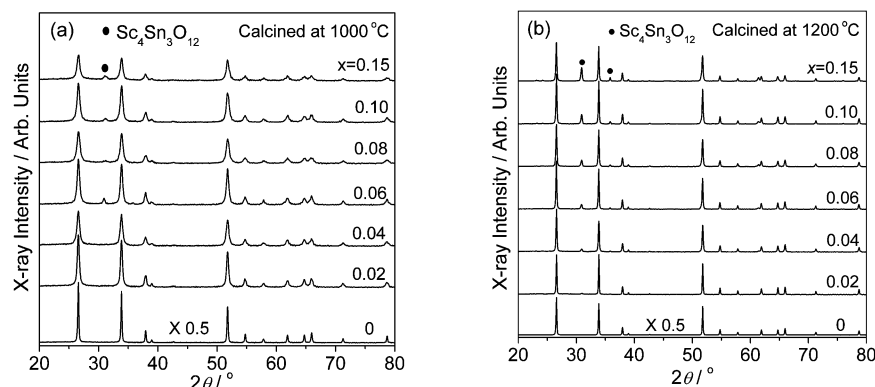


Figure 9. XRD patterns of $(\text{SnO}_2)_{1-x}(\text{Sc}_2\text{O}_3)_x$ ($x = 0\text{--}0.15$) powders calcined at (a) 1000 °C and (b) 1200 °C for 2 h. (●) Hexagonal $\text{Sc}_4\text{Sn}_3\text{O}_{12}$.

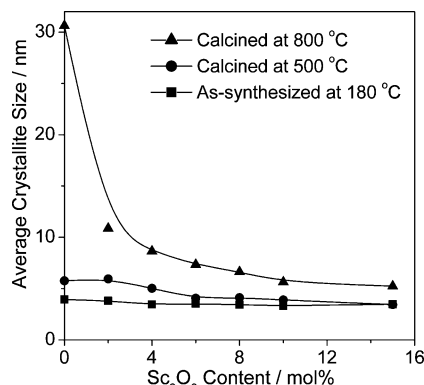


Figure 10. Average crystallite size of the nanocrystalline $(\text{SnO}_2)_{1-x}(\text{Sc}_2\text{O}_3)_x$ ($x = 0-0.15$) powders as a function of the Sc_2O_3 content.

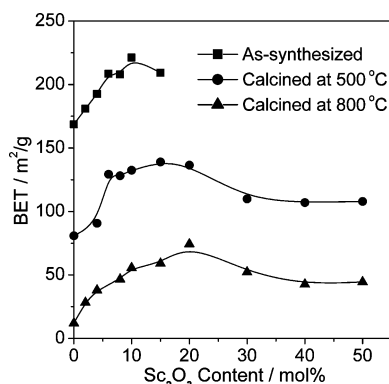


Figure 11. BET specific surface area of the nanocrystalline $(\text{SnO}_2)_{1-x}(\text{Sc}_2\text{O}_3)_x$ ($x = 0-0.5$) powders as a function of the Sc_2O_3 content.

HRTEM measurements were conducted to characterize the morphology and structure of the as-calcined powders. A typical HRTEM image of the sample with $x = 0.10$ calcined at $800\text{ }^\circ\text{C}$, shown in Figure 12a, indicates that the nanoparticles exhibit a relatively uniform rectangle morphology (with average grain size of ca. 6 nm). The clear lattice fringes in the HRTEM image confirm the single crystalline nature of the nanoparticles. The spacing between the adjacent lattice fringes is 0.333 nm , corresponding to the (110) facet of tetragonal SnO_2 . The HRTEM lattice image of the sample with $x = 0.20$ calcined at $800\text{ }^\circ\text{C}$ is shown in Figure 12b. Both the (110) facet of tetragonal SnO_2 ($d = 0.337\text{ nm}$) and the (222) facet of cubic Sc_2O_3 ($d = 0.285\text{ nm}$) can be distinguished, indicating the segregation of Sc_2O_3 crystals at the grain boundary of SnO_2 , which is conformed with the result of XRD (Figure 4b). Furthermore,

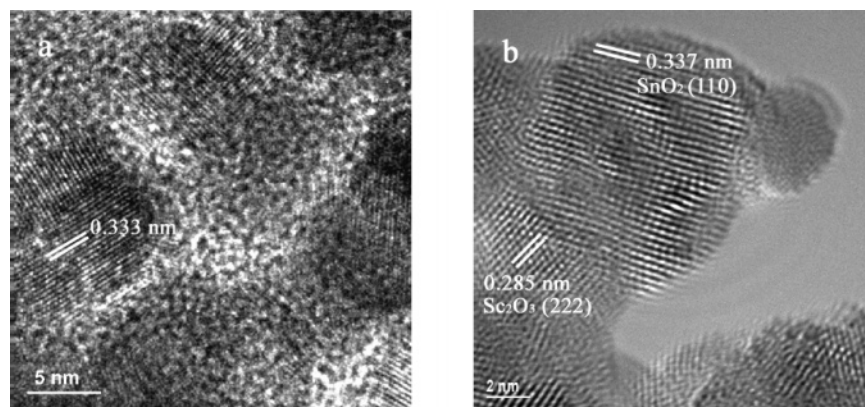


Figure 12. HRTEM images of $(\text{SnO}_2)_{1-x}(\text{Sc}_2\text{O}_3)_x$ nanocrystals calcined at $800\text{ }^\circ\text{C}$ for 2 h. (a) $x = 0.1$; (b) $x = 0.2$.

the lattice fringes of the sample with $x = 0.2$ are significantly distorted (see Figure 12b), which implies that a high level of strain still remains in the SnO_2 lattice, which is in accordance with the fact that this sample possesses the highest microstrain at the calcination temperature of $800\text{ }^\circ\text{C}$ (see Figure 3S of Supporting Information). It is evident that the adulteration of Sc_2O_3 can affect the crystallization of SnO_2 and bring more distorted lattices to it under the present experimental conditions.

5. Schematic Diagram for the Phase Evolution of $(\text{SnO}_2)_{1-x}(\text{Sc}_2\text{O}_3)_x$. To take full consideration of the above results obtained by XRD, crystallite size determination, HRTEM measurement, and Raman and XPS analysis, we describe the phasic dependence of the $(\text{SnO}_2)_{1-x}(\text{Sc}_2\text{O}_3)_x$ ($x = 0.02-0.6$) powders upon the calcining temperature/particle size by a scheme in Figure 13. At the low level doping ($x = 0.02-0.1$), the tetragonal structure of the as-synthesized $(\text{SnO}_2)_{1-x}(\text{Sc}_2\text{O}_3)_x$ nanocrystallites is stable up to $800\text{ }^\circ\text{C}$ and tends to segregate a second layer of $\text{Sc}_4\text{Sn}_3\text{O}_{12}$ after calcination at higher temperatures to $1200\text{ }^\circ\text{C}$. It should be noted that a metastable $(\text{SnO}_2)_{1-x}(\text{Sc}_2\text{O}_3)_x$ solution exists for the samples with $x = 0.02-0.06$ after calcining at $800\text{ }^\circ\text{C}$. At the middle level doping ($x = 0.15-0.3$), the as-synthesized $(\text{SnO}_2)_{1-x}(\text{Sc}_2\text{O}_3)_x$ nanocrystallites appear a mixed phase of tetragonal SnO_2 and a portion of $\alpha\text{-ScOOH}$. When calcining at $800\text{ }^\circ\text{C}$, the phasic mixture of tetragonal phase plus cubic Sc_2O_3 is observable. Upon further calcination at temperatures higher than $1200\text{ }^\circ\text{C}$, an increasing amount of $\text{Sc}_4\text{Sn}_3\text{O}_{12}$ is formed along with the tetragonal phase. At the high level doping ($x = 0.4-0.6$), the as-synthesized $(\text{SnO}_2)_{1-x}(\text{Sc}_2\text{O}_3)_x$ nanocrystallites display a mixed phase of tetragonal SnO_2 and a considerable amount of $\alpha\text{-ScOOH}$. During calcination at $800\text{ }^\circ\text{C}$, a mixture of tetragonal phase plus cubic Sc_2O_3 is present. Upon further calcination at temperatures higher than $1200\text{ }^\circ\text{C}$, a single phase of $\text{Sc}_4\text{Sn}_3\text{O}_{12}$ will be obtained (also see Figure 4S).

6. Correlation between the CO Gas-Sensing Property and the Structure/Texture. The $(\text{SnO}_2)_{1-x}(\text{Sc}_2\text{O}_3)_x$ ($x = 0-0.15$) pellets sintered at $800\text{ }^\circ\text{C}$ for 24 h are composed of uniform and well-crystallized nanocrystals with a grain size of ca. 30 and 10 nm for $x = 0$ and 0.06, respectively (see Figure 5S). The CO sensitivity ($R_{\text{air}}/R_{\text{CO}}$) of the as-sintered pellets were examined with complex impedance measurement in air and in 1000 ppm CO (see Figure 6S) at a substrate temperature varying from 250 to $450\text{ }^\circ\text{C}$. Figure 14 shows the dynamic variation of sensitivity with operating time at various operation temperatures, T_{op} , for the as-sintered $(\text{SnO}_2)_{0.90}(\text{Sc}_2\text{O}_3)_{0.10}$ pellet. When the CO was introduced, the sensitivity increased significantly with the operation time, especially when the T_{op} exceeded $300\text{ }^\circ\text{C}$.

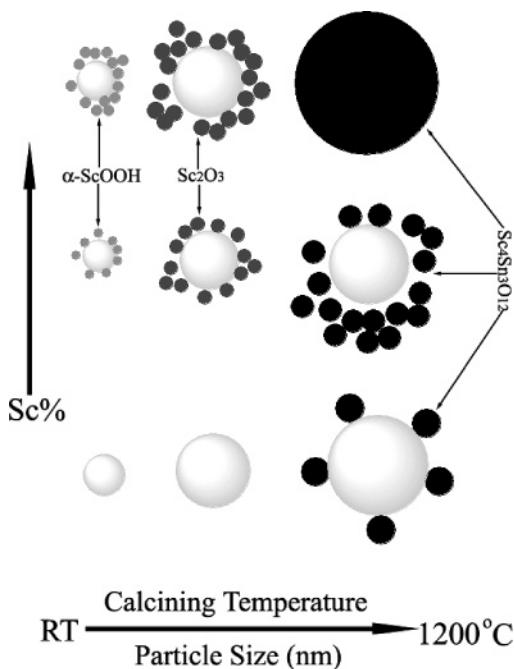


Figure 13. Schematic diagram for the phasic dependence of the $(\text{SnO}_2)_{1-x}(\text{Sc}_2\text{O}_3)_x$ ($x = 0.02\text{--}0.6$) nanocrystallites upon the calcination temperature/particle size (RT, room temperature).

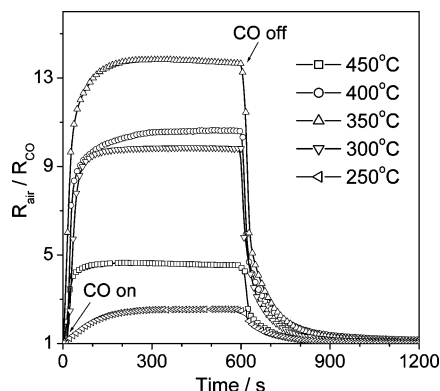


Figure 14. Effect of operation temperature on the sensitivity in 1000 ppm CO for the as-sintered $(\text{SnO}_2)_{0.90}(\text{Sc}_2\text{O}_3)_{0.10}$ pellet.

The response time, at which the sensitivity attains 90% of the stabilized value, for the as-sintered $(\text{SnO}_2)_{0.90}(\text{Sc}_2\text{O}_3)_{0.10}$ pellet at T_{op} of 350 °C is ca. 70 s and is much lower than that of pure SnO_2 (210 s; this work). Furthermore, as the CO was turned off, the sensitivity of the as-sintered pellets fell rapidly, indicating that the good recovery of the resistance was obtained for the present sample. The recovery of the resistance when the CO is removed is determined by both oxygen readsorption from the ambient at the surface and reoxidation of the oxide.⁶ By assumption that the CO was excluded completely when the gas was turned off, the residual CO could be neglected. Therefore, the rapid recovery of the sensitivity for the as-sintered pellet may be caused by the easy adsorption of oxygen due to the small grain size and rich grain boundaries it has.

Figure 15 depicts the sensitivity in 1000 ppm CO at various operation temperatures for the as-sintered $(\text{SnO}_2)_{1-x}(\text{Sc}_2\text{O}_3)_x$ ($x = 0\text{--}0.15$) pellets. It is noted that the sensitivity does not exhibit a significant difference for all the samples at the T_{op} of 250 °C. For $x < 0.04$, the maximum sensitivity happens at the T_{op} of 400 °C, whereas the T_{op} of the maximum sensitivity shifts to 350 °C for $x > 0.04$. At a low operation temperature, the low sensitivity can be expected because the CO molecules do

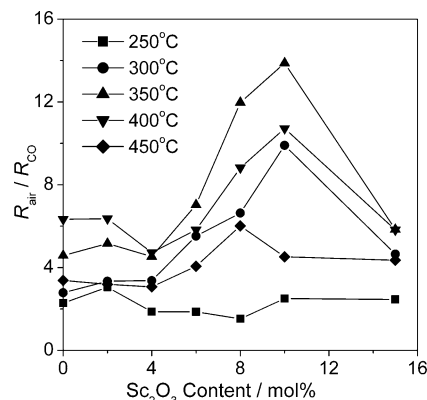
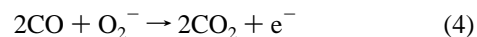
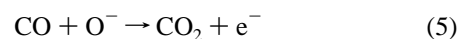


Figure 15. Effect of the sensitivity in 1000 ppm CO at various operation temperatures for the as-sintered $(\text{SnO}_2)_{1-x}(\text{Sc}_2\text{O}_3)_x$ ($x = 0\text{--}0.15$) pellets vs the Sc_2O_3 content.

not have enough thermal energy to react with the surface adsorbed oxygen species, O_2^- , i.e., the reaction rate of eq 4 is essentially low⁴⁴



As T_{op} is increased to 300 °C, the adsorbed oxygen is converted from O_2^- to O^- , and the CO sensing reaction can be expressed as eq 5⁴⁴



The increase in sensitivity for T_{op} above 300 °C can be attributed to the fact that the thermal energy obtained is high enough to overcome the activation energy barrier to the reaction, and a significant increase in electron concentration results from the sensing reaction as shown in eq 4. The maximum sensitivity of 13.9 is found for $x = 0.10$ at 350 °C of T_{op} . While the reduction in sensitivity above 350 °C of T_{op} was due to the difficulty in exothermic CO gas adsorption, an optimum operation temperature should be considered for obtaining a high sensitivity when using the present $(\text{SnO}_2)_{1-x}(\text{Sc}_2\text{O}_3)_x$ nanomaterials in CO gas sensing devices.

It is also interesting to note from Figure 15 that, in the T_{op} range of 300–400 °C, the sensitivity for $x < 0.06$ does not show obvious variation, but increases sharply as $x > 0.06$ and reaches a maximum for $x = 0.10$ and decreases thereafter. Therefore, the sample with $x = 0.1$ shows the best CO gas-sensing property in the T_{op} range of 300–400 °C among all the samples tested. The above gas-sensing property can be well correlated with the structure and textural characteristics of the $(\text{SnO}_2)_{1-x}(\text{Sc}_2\text{O}_3)_x$ sensors as discussed above. It is well-known that the sensitivity of the metal–oxide semiconductor sensors is mainly determined by the interactions between the target gas and the surface of the sensors. The reduction of the grain size with the increase of x (see Figure 5S) leads to the increase of the total surface area and grain boundary of the samples. The larger number of adsorption–desorption sites it provides, the higher sensitivity can be achieved by the significant change in the surface interaction. Note that the conductivity of the sensor material is more sensitive to the surface than the bulk; the small difference of the sensitivities for the samples containing less than 6 mol % Sc_2O_3 would probably be due to the formation of the solid solution structure. The maximum sensitivity is observed for $x = 0.10$, perhaps as a result of the largest amount of active reaction sites (surface defects) led by the random dispersion of Sc on the SnO_2 grains at this composition, as revealed by the

above structural analysis. The abrupt decrease of the sensitivity for the samples with $x > 0.15$ is probably due to the reduction of active sites correlated with the segregation of more Sc_2O_3 grains.

Conclusions

By a two-step urea homogeneous precipitation hydrothermal method, weakly agglomerated nanocrystalline scandia doped tin oxide powders with high surface area (170–220 m^2/g) and small crystallite size (3–4 nm) were synthesized. Refinement of the lattice parameter, the linear red shift of the Raman peaks, as well as the determination of surface Sc/Sn ratio by XPS show that a metastable scandium tin oxide solid solution in tetragonal structure has been formed for the Sc dopant content lower than 6 mol % as the samples were calcined at 800 °C. Above this limit, the excess Sc randomly disperses at the surfaces of the nanocrystallites. When calcined at high temperatures (>1000 °C), Sc is inclined to move from the interior of SnO_2 grains to the surface region and react with SnO_2 to form the compound $\text{Sc}_4\text{Sn}_3\text{O}_{12}$. For higher dopant concentration (>15 mol %), $\alpha\text{-ScOOH}$ is segregated from the as-synthesized samples, while Sc_2O_3 is precipitated from the as-calcined samples. It is inferred that the high-temperature calcination tends to promote the segregation of Sc from SnO_2 grain interiors for a given composition. Furthermore, the presence of the doped and dispersed Sc has a significant effect on the grain growth and the crystallizing process. The average grain size of the samples calcined at 800 °C decreases abruptly as the increase of the dopant concentration. The specific surface area in the as-synthesized and as-calcined powders increase along with the dopant concentration and reach a maximum at the dopant content of ca. 20 mol %. In the case of the samples with higher dopant concentration, the precipitated $\alpha\text{-ScOOH}$ or Sc_2O_3 does not influence the specific surface area of the samples obviously.

The structural and textural characteristics of the as-calcined $(\text{SnO}_2)_{1-x}(\text{Sc}_2\text{O}_3)_x$ can be well correlated with the CO sensing property. The doping of Sc has reduced the optimum operation temperature from 400 to 350 °C. Moreover, at the operation temperature range of 300–400 °C, the sensitivity for $x < 0.06$ in a solid solution structure does not show obvious variation but increases sharply as $x > 0.06$ and reaches a maximum for $x = 0.10$ due to the fact that the dispersion of scandium on the surface of the grains hinders the crystallite growth and brings larger surface area. The precipitation of more Sc_2O_3 results in the reduction of the sensitivity as $x > 0.15$. Therefore, the pellet sample with scandia content of 10 mol % sintered at 800 °C showed the best CO gas-sensing property in the operation temperature range of 300–400 °C. It is also worthwhile to note that the as-presented results have provided us a systematic comprehension of the correlation between the structural/textural characteristics and the CO gas-sensing property in the nanocrystalline $\text{SnO}_2\text{--Sc}_2\text{O}_3$ system. The as-prepared nanocrystalline Sc_2O_3 -doped SnO_2 nanocrystalline powders promise good candidate materials in CO gas sensors at the composition of 10 mol % Sc_2O_3 and may find use in other applications such as catalysis. Furthermore, it is expected that the present study can bring some useful information on designing novel multicomponent oxides materials with specific structure and desirable properties.

Acknowledgment. We gratefully acknowledge the financial support from NSFC (Grant Nos. 20171003, 20221101, 20490210, and 20423005) and the National Postdoctoral Fellow Fund of China (Grant No. 2003033063).

Supporting Information Available: Rietveld refinement of the $(\text{SnO}_2)_{1-x}(\text{Sc}_2\text{O}_3)_x$ ($x = 0\text{--}0.15$) powders calcined at 800 °C for 24 h (Figure 1S), XPS patterns of $(\text{SnO}_2)_{1-x}(\text{Sc}_2\text{O}_3)_x$ ($x = 0\text{--}0.15$) powders calcined at 800 °C (Figure 2S), microstrain in the nanocrystalline $(\text{SnO}_2)_{1-x}(\text{Sc}_2\text{O}_3)_x$ ($x = 0\text{--}0.50$) powders as a function of Sc_2O_3 content (Figure 3S), XRD patterns of $(\text{SnO}_2)_{1-x}(\text{Sc}_2\text{O}_3)_x$ ($x = 0.20\text{--}0.50$) powders calcined at 1200 °C (Figure 4S), SEM micrographs of $(\text{SnO}_2)_{1-x}(\text{Sc}_2\text{O}_3)_x$ ($x = 0, 0.06$) pellets sintered at 800 °C for 24 h (Figure 5S), and typical complex impedance spectra of the as-sintered $(\text{SnO}_2)_{0.90}(\text{Sc}_2\text{O}_3)_{0.10}$ pellet examined at 350 °C in air and in 1000 ppm CO (Figure 6S). This material is available free of charge via the Internet at <http://pubs.acs.org>.

References and Notes

- Albery, W. J.; Archer, M. D. *Nature* **1977**, 270, 399.
- Ferrere, S.; Zaban, A.; Gregg, B. A. *J. Phys. Chem. B* **1997**, 101, 4490.
- Harrison, P. G.; Bailey, C.; Azelee, W. J. *Catal.* **1999**, 186, 147.
- He, Y. S.; Campbell, J. C.; Murphy, R. C.; Arendt, M. F.; Swinnea, J. S. *J. Mater. Res.* **1993**, 8, 3131.
- Seiyama, T.; Kato, A.; Fujiishi, K.; Nagatani, M. *Anal. Chem.* **1962**, 34, 1052.
- Ihokura, K.; Watson, J. *The Stannic Oxide Gas Sensor: principle and Applications*; CRC Press: Boca Raton, 1994.
- Xu, C.; Tamaki, J.; Miura, N.; Yamazoe, N. *Sens. Actuators B* **1991**, 3, 147.
- Morris, L.; Williams, D. E. *J. Phys. Chem. B* **2001**, 105, 7272.
- Tsang, S. C.; Bulpitt, C. D. A.; Mitchell, P. C. H.; Ramirez-Cuesta, A. J. *J. Phys. Chem. B* **2001**, 105, 5737.
- Chowdhuri, A.; Gupta, V.; Sreenivas, K. *Sens. Actuators B* **2003**, 93, 572.
- Choi, U. S.; Sakai, G.; Shimano, K.; Yamazoe, N. *Sens. Actuators B* **2004**, 98, 166.
- Sorescu, M.; Diamandescu, L.; Tarabasanu-Mihaila, D.; Teodorescu, V. S.; Howard, B. H. *J. Phys. Chem. Solids* **2004**, 65, 1021.
- Gourari, H.; Lumberras, M.; Landschoot, R.; Van Schoonman, J. *Sens. Actuators B* **1998**, 47, 189.
- Ansari, Z. A.; Ansari, S. G.; Ko, T.; Oh, J. H. *Sens. Actuators B* **2002**, 87, 105.
- Reddy, C. V. G.; Manorama, S. V.; Rao, V. J. *J. Mater. Sci.* **2000**, 35, 3403.
- Khodadadi, A.; Mohajerzadeh, S. S.; Mortazavi, Y.; Miri, A. M. *Sens. Actuators B* **2001**, 80, 267.
- Weber, I. T.; Maciel, A. P.; Lisboa, P. N.; Longo, E.; Leite, E. R. *Nano Lett.* **2002**, 2, 969.
- Carreno, N. L. V.; Maciel, A. P.; Leite, E. R.; Lisboa, P. N.; Longo, E.; Valentini, A.; Probst, L. F. D.; Paiva-Santos, C. O.; Schreiner, W. H. *Sens. Actuators B* **2002**, 86, 185.
- Schweizer-Berberich, M.; Zheng, J. G.; Weimar, U.; Göpel, W.; Bärsan, N.; Pentia, E.; Tomescu, A. *Sens. Actuators B* **1996**, 31, 71.
- Lim, C. B.; Oh, S. *Sens. Actuators B* **1996**, 30, 223.
- Herrmann, J. M.; Disdier, J.; Fernández, A.; Jiménez, V. M.; Sánchez-López, J. C. *Nanostruct. Mater.* **1997**, 8, 675.
- Jiménez, V. M.; González-Elipe, A. R.; Espinós, J. P.; Justo, A.; Fernández, A. *Sens. Actuators B* **1996**, 31, 29.
- Yu, K. N.; Xiong, Y. H.; Liu, Y. L.; Xiong, C. S. *Phys. Rev. B* **1997**, 55, 2666.
- Egashira, M.; Shimizu, Y.; Takao, Y.; Fukuyama, Y. *Sens. Actuators B* **1996**, 33, 89.
- Liu, Y.; Zhu, W.; Tan, O. K.; Yao, X.; Shen, Y. *J. Mater. Sci.: Mater. Electron.* **1996**, 7, 279.
- Shannon, R. D. *Acta Crystallogr.* **1976**, A32, 751.
- Xu, G.; Zhang, Y. W.; Liao, C. S.; Yan, C. H. *J. Am. Ceram. Soc.* **2002**, 85, 995.
- Zhang, Y. W.; Xu, G.; Yan, Z. G.; Yang, Y.; Liao, C. S.; Yan, C. H. *J. Mater. Chem.* **2002**, 12, 970.
- Larson, A. C.; von Dreele, R. B. *Report LAUR 86-748*; Los Alamos National Laboratory, 1986.
- Guinier, A. *Theorie et Technique de la Radiocristallographie*, 3rd ed.; Dunod: Paris, 1964; p 482.
- Dekeijser, T. H.; Langford, J. I.; Mittemeijer, E. J.; Vogels, A. B. *P. J. Appl. Cryst.* **1982**, 15, 308.
- Epifani, M.; Alvisi, M.; Mirengi, L.; Leo, G.; Siciliano, P.; Vasanelli, L. *J. Am. Ceram. Soc.* **2001**, 84, 48.
- Xie, Y. C.; Tang, Y. Q. *Adv. Catal.* **1990**, 37, 1.
- Diéguez, A.; RomanoRodríguez, A.; Morante, J. R.; Weimar, U.; SchweizerBerberich, M.; Göpel, W. *Sens. Actuators B* **1996**, 31, 1.

- (35) Abello, L.; Bochu, B.; Gaskov, A.; Koudryavtseva, S.; Lucazeau, G.; Roumyantseva, M. *J. Solid State Chem.* **1998**, *135*, 78.
- (36) Zuo, J.; Xu, C.; Y.; Liu, X. M.; Wang, C. S.; Wang, C. Y.; Hu, Y.; Qian, Y. T. *J. Appl. Phys.* **1994**, *75*, 1835.
- (37) Xie, C. Y.; Zhang, L. D.; Mo, C. M. *Phys. Status Solidi A* **1994**, *141*, K59.
- (38) Porto, S. P. S.; Fleury, P. A.; Damen, T. C. *Phys. Rev.* **1967**, *154*, 522.
- (39) Scott, J. F. *J. Chem. Phys.* **1970**, *53*, 852.
- (40) Santilli, C. V.; Pulcinelli, S. H.; Brito, G. E. S.; Briois, V. *J. Phys. Chem. B* **1999**, *103*, 2660.
- (41) Davis, S. R.; Chadwick, A. V.; Wright, J. D. *J. Phys. Chem. B* **1997**, *101*, 9901.
- (42) Dusastre, V.; Williams, D. E. *J. Phys. Chem. B* **1998**, *102*, 6732.
- (43) Slater, B.; Catlow, C. R. A.; Gay, D. H.; Williams, D. E.; Dusastre, V. *J. Phys. Chem. B* **1999**, *103*, 10644.
- (44) Aroutiounian, V. M.; Aghababian, G. S. *Sens. Actuators B* **1998**, *50*, 80.